Large Format Long-Wavelength Infrared Narrow-Band, Multi-Band, and Broad-Band QWIP Focal Plane Arrays

S. D. Gunapala, S. V. Bandara, J. K. Liu, S. B. Rafol, and J. M. Mumolo
Jet Propulsion Laboratory, California Institute of Technology, 4800 Oak Grove Drive, Pasadena, CA 91109, USA

ABSTRACT

A 640x512 pixel, long-wavelength cutoff, narrow-band ($\Delta\lambda/\lambda$~10%) quantum well infrared photodetector (QWIP) focal plane array (FPA), a four-band QWIP FPA in 4-16 μm spectral region, and a broad-band ($\Delta\lambda/\lambda$~42%) QWIP FPA having 15.4 μm cutoff have been demonstrated. In this paper we discuss the detector designs, dark currents, quantum efficiencies, responsivities, detectivities, noise equivalent differential temperatures (NEDTs), the effect of FPA nonuniformity on performance, and the operabilities of these QWIP FPAs. In addition, we discuss the development of a very sensitive (NEDT~10.6 mK) 640x512 pixel thermal imaging camera having 9 μm cutoff.

Index Terms: Infrared, long-wavelength infrared, mid-wavelength infrared, narrow-band infrared, multi-band infrared, broad-band infrared, infrared imaging camera, focal plane array, quantum well infrared photodetectors.

I. INTRODUCTION

The physics of reduced dimensionality in semi-conductor quantum structures results in innovative device concepts, enabling electronic and opto-electronic devices with enhanced performances. The quantum well infrared photodetector (QWIP) is a successfully demonstrated device based on intersubband photoexcitation occurring in one-dimensionally confined quantum structures. Energy levels in the quantum well are quantized only in one direction, while they are continuous in the other two directions. The idea of using multi-quantum-well (MQW) structures to detect infrared radiation (i.e., QWIP) can be explained by using the basic principles of quantum mechanics. The design and optimization of MQW based infrared detectors are described in detail elsewhere [1-15].

The QWIPs discussed in this article utilize the photoexcitation of electrons (holes) between the ground state and the first excited state in the conduction (valance) band quantum well (see Fig. 1). The quantum well structure is designed so that these photoexcited carriers can escape from the quantum well and be collected as photocurrent. In addition to larger intersubband oscillator strength, these detectors afford greater flexibility than extrinsically doped semiconductor infrared detectors because the peak wavelength of the response, cutoff wavelength, and the spectral width of the response can be continuously tailored by varying layer thickness (quantum well width) and barrier composition (barrier height). The position of the energy levels are primarily determined by the quantum well dimensions (height and width). For infinitely high barriers and parabolic bands, the energy levels in the quantum well are given by

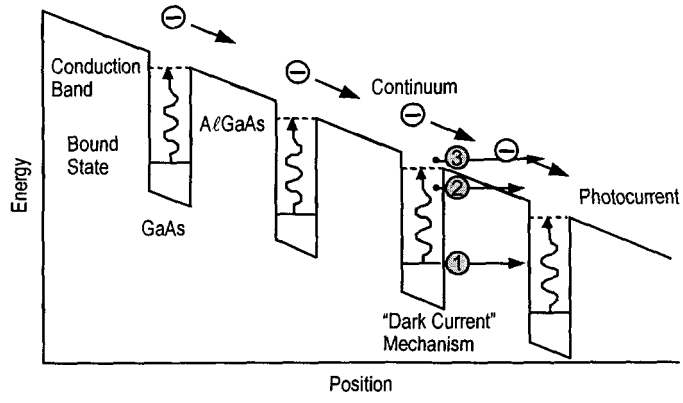

Fig. 1. Schematic diagram of the conduction band in a bound-to-quasibound QWIP in an externally applied electric field. Absorption of IR photons can photoexcite electrons from the ground state of the quantum well into the continuum, causing a photocurrent. Three dark current mechanisms are also shown: ground state tunneling (1); thermally assisted tunneling (2); and thermionic emission (3).

$$E_j = \left(\frac{\hbar^2 \pi^2}{2m^* L_w^2}\right) j^2, \quad (1)$$

where L_W is the width of the quantum well, m^* is the effective mass of the carrier in the quantum well, and j is an integer. Thus, the intersubband energy between the ground and the first excited state is

$$(E_2 - E_1) = (3\hbar^2\pi^2 / 2m^*L_w^2). \quad (2)$$

The lattice-matched GaAs/$Al_xGa_{1-x}As$ material system is a very good candidate to create such a quantum well structure, because the band gap of $Al_xGa_{1-x}As$ can be changed continuously by varying x (and hence the height of the quantum well). Thus, by changing the quantum well width L_W and the barrier height (Al molar ratio of $Al_xGa_{1-x}As$ alloy), this intersubband transition energy can be varied over a wide range, from the mid-wavelength infrared (MWIR; 3-5 μm), through long-wavelength infrared (LWIR; 8-12 μm), and into the very long-wavelength infrared (VLWIR; >12 μm). It is important to note that unlike intrinsic detectors, which utilize interband transition, quantum wells of these detectors must be doped since the photon energy is not sufficient to create photocarriers ($h\upsilon < E_g$).

There has been much interest lately [1-15] in large format QWIP focal plane arrays (FPAs). In this paper we discuss the design, fabrication, and test results of a 640x512 pixel narrow-band QWIP FPA. A very sensitive portable LWIR camera has also been demonstrated based on this LWIR FPA. In addition, we discuss the first demonstration of four-band and broad-band QWIP FPAs in the 4-16 μm spectral region. These large format FPAs will be useful for many applications, such as the in-situ and remote sensing of gas molecules, thermal imaging, global atmospheric temperature profiles monitoring, cloud characteristics measurements, astronomy, tracking and identification of missiles, etc.

II. NARROW-BAND QWIP DEVICE

Each period of the MQW structure consists of a 45 Å well of GaAs (doped $n = 5x10^{17}$ cm^{-3}) and a 500 Å barrier of $Al_{0.3}Ga_{0.7}As$. Stacking many identical quantum wells (typically 50) together increases photon absorption. Ground state electrons are provided in the detector by doping the GaAs well layers with Si. This photosensitive MQW structure is sandwiched between 0.5 μm GaAs top and bottom contact layers doped $n = 5x10^{17}$ cm^{-3}, grown on a semi-insulating GaAs substrate by molecular beam epitaxy (MBE). Then a 0.7 μm thick GaAs cap layer on top of a 300 Å $Al_{0.3}Ga_{0.7}As$ stop-etch layer was grown in-situ on top of the device structure to fabricate the light coupling optical cavity. The MBE grown material was tested for absorption efficiency using a Fourier Transform Infrared (FTIR) spectrometer. Figure 2 shows the measured absorption quantum efficiency of this material at room temperature. The epitaxially grown material was processed into 200 μm diameter mesa test structures (area = $3.14x10^{-4}$ cm^2) using wet chemical etching, and Au/Ge ohmic contacts were evaporated onto the top and bottom contact layers. The dark current of this test device was measured as a function of the device operating temperature with bias at –1.1 V across the device (see Fig. 3).

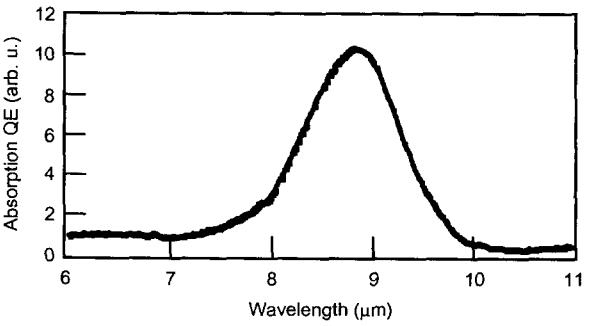

Fig. 2. Absorption quantum efficiency of the QWIP material at room temperature.

The detectors were back illuminated through a 45° polished facet [5] for optical characterization and an experimentally measured responsivity spectrum is shown in Fig. 4. The responsivity of the detector peaks at 8.5 μm and the peak responsivity (R_P) of the detector is 83 mA/W at bias V_B = –1.1 V. The spectral width and the cutoff wavelength are $\Delta\lambda/\lambda$ = 10% and λ_c = 8.9 μm, respectively. The measured absolute peak responsivity of the detector is small, up to about V_B = –0.5 V. Beyond that it increases nearly linearly with bias, reaching R_P = 420 mA/W at V_B = –5 V. This type of behavior of responsivity versus bias is typical for a bound-to-quasibound QWIP. The net peak quantum efficiency was 1.4% at bias V_B = –1.1 V for a 45° double pass. The lower quantum efficiency is due to the lower photoconductive gain at lower operating bias. Lower operating bias suppresses the

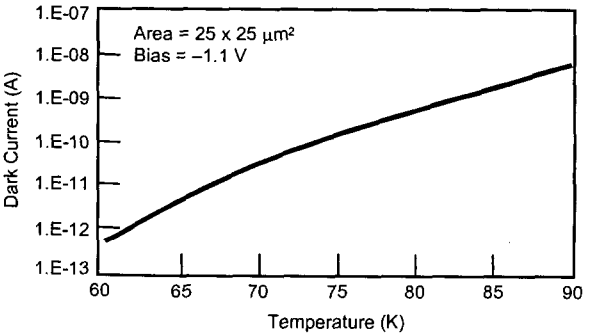

Fig. 3. Dark current of 8.5 μm peaked bound-to-quasibound QWIP as a function of temperature. Data were taken with a 200 μm diameter test structure and normalized to 25x25 μm^2 pixel.

dark current. Due to limited readout multiplexer well depth (i.e., $11x10^6$ electrons), it is preferred to have a lower dark current to achieve a higher operating temperature and longer integration times. In background limited performance (BLIP) conditions, the noise equivalent differential temperature (NEDT) improves with the increasing integration time. In this case, the lowest operating temperature of 65 K was determined by the cooling capacity of the small Stirling cooler used in an Indigo Phoenix™ camera.

The photoconductive gain g was experimentally determined using [3] $g = i_n^2 / 4eI_D\Delta f + 1/(2N)$, where Δf is the measurement bandwidth, N is the number of quantum wells, and i_n is the current noise, which was measured using a spectrum analyzer. The photoconductive gain of the detector reached 0.98 at $V_B = -5$ V. Since the gain of QWIP is inversely proportional to the number of quantum wells N, the better comparison would be the well capture probability p_c, which is directly related to the gain [3] by $g = 1/(Np_c)$. The calculated well capture probabilities are 25% at low bias (i.e., $V_B = -1$ V) and 2% at high bias (i.e., $V_B = -5$ V), which together indicate the excellent hot-electron transport in this device structure. The peak detectivity is defined as $D_P^* = R_P \sqrt{A\Delta f} / i_n$, where R_P is the peak responsivity, A is the area of the detector and $A = 3.14x10^{-4}$ cm^2. The measured peak detectivity at bias $V_B = -1.1$ V and temperature T = 65 K is $1x10^{11}$ cm$\sqrt{\text{Hz}}$ /W. Figure 5 shows the bias dependence of peak detectivity as a function of temperature. These detectors show BLIP at bias $V_B = -2$ V and temperature T = 72 K for a 300 K background with f/2 optics.

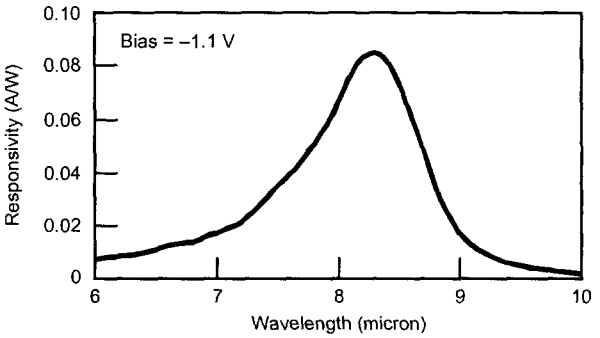

Fig. 4. Responsivity spectrum of a bound-to-quasibound LWIR QWIP test structure at temperature T = 77 K. The spectral response peak is at 8.5 μm and the long wavelength cutoff is at 8.9 μm.

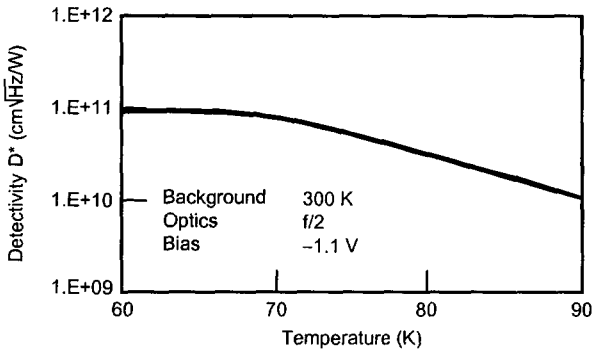

Fig. 5. Detectivity as a function of temperatures at bias of -1.1 V.

III. DETECTIVITY D* COMPARISON

The blackbody detectivity D_B^* is basically the signal-to-noise ratio of a radiation detector normalized to unit area and operating bandwidth of the detector and is given by,

$$D_B^* = R_B \frac{\sqrt{A\Delta f}}{i_n} \tag{3}$$

with

$$R_B = \frac{\int_{\lambda 1}^{\lambda 2} R(\lambda)W(\lambda)d\lambda}{\int_{\lambda 1}^{\lambda 2} W(\lambda)d\lambda}, \tag{4}$$

where the responsivity R can be written in terms of quantum efficiency η and photoconductive gain g as

$$R = (e/h\nu)\eta_a g. \tag{5}$$

The photoconductive gain of QWIPs can be written as

$$g = L/l, \tag{6}$$

where L is the hot electron mean free path, and the l is the length of the MQW region. The temporal noise current i_n of a single element radiation detector is given by,

$$i_n = \sqrt{\beta e(I_D + I_P)g\Delta f}\,, \tag{7}$$

where e is the charge of an electron, β=2 for a photovoltaic detector (generation only) and β=4 for a photoconductor (generation and recombination), the photoconductive gain g = 1 for a photovoltaic detector and g(QWIP) is typically 0.2 to 0.5 (depends on the device structure). I_D is the detector dark current and I_P is the detector photocurrent, given by,

$$I_P = e\eta_a g\Phi A \tag{8}$$

where Φ is the photon flux, (see reference 3 for details).

Let's consider a background limited condition. At this condition

$$I_D < I_P \tag{9}$$

By combining equations (3), (5), (6), (7), (8), and (9) the detectivity D* can be written as,

$$D^* = \frac{1}{h\nu}\sqrt{\frac{\eta_a}{\beta\Phi}} \tag{10}$$

Thus,

$$\frac{D^*_{IDEAL}}{D^*_{QWIP}} = \sqrt{\frac{2\eta_{a,IDEAL}}{\eta_{a,QWIP}}} \tag{11}$$

The lowest absorption quantum efficiency (η_a) of QWIP is typically 15% (including 30% reflection loss). The η_a of an ideal detector is 70% (assume 30% reflection loss). Thus equation (11) reduces to,

$$\frac{D^*_{IDEAL}}{D^*_{QWIP}} = 2.67 \tag{12}$$

This analysis clearly shows the photoconductive gain is not very important at BLIP operating conditions, and therefore, the detectivities scale solely as a function of absorption quantum efficiencies (net quantum efficiency/photoconductive gain) of the detectors.

IV. 640x512 PIXEL NARROW-BAND FOCAL PLANE ARRAY

QWIPs do not absorb radiation incident normal to the surface since the light polarization must have an electric field component parallel to the MQW (growth direction) to be absorbed by the confined carriers [3]. However, this difficulty can easily overcome by fabricating light coupling structures such as gratings or randomly roughened reflectors on top of each detector pixels. Although random reflectors [4] have achieved relatively high quantum efficiencies with large test device structures, it is difficult to fabricate random reflectors for shorter wavelength detectors relative to very long-wavelength detectors (i.e., 15 μm), because the feature sizes of random reflectors are linearly proportional to the peak wavelength of the detectors [10]. For example, the minimum feature sizes of the random reflectors for 15 μm cutoff and 9 μm cutoff FPAs were 1.25 and 0.6 μm, respectively. It is difficult to fabricate these sub-micron features by contact photolithography. As a result, the random reflectors of the 9 μm cutoff FPA were less sharp and had fewer scattering centers compared to those of the 15 μm cutoff QWIP FPA. As we have discussed before [11,15], more IR light can be coupled to the QWIP detector structure by incorporating a two-dimensional grating surface on top of the detectors which also removes the light coupling limitations and makes two-dimensional QWIP imaging arrays feasible. This two-dimensional grating structure was fabricated on the detectors by using standard photolithography and Cl_2-based reactive ion etching.

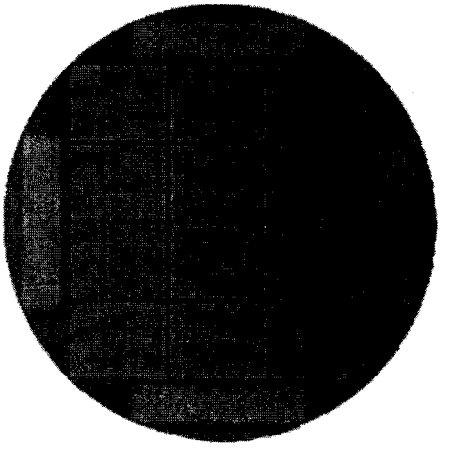

Fig 6. Twelve 640x512 QWIP focal plane arrays on a 3 inch GaAs wafer.

After the two-dimensional grating array was defined by the lithography and reactive ion etching, the photoconductive QWIPs of the 640x512 pixel

FPAs were fabricated by dry etching through the photosensitive GaAs/$Al_xGa_{1-x}As$ multi-quantum well layers into the 0.5 μm thick doped GaAs bottom contact layer. The detector pixel pitch of the FPA is 25 μm and the actual pixel area is 23x23 μm^2. The two-dimensional gratings on top of the detectors were then covered with Au/Ge and Au for Ohmic contact and reflection of non-absorbed infrared radiation back into the photosensitive MQW region. Figure 6 shows twelve processed 640x512 pixel QWIP FPAs on a 3 inch GaAs wafer. Indium bumps were then evaporated on top of the detectors for hybridization with a silicon readout integrated circuit (ROIC). A single QWIP FPA was chosen and hybridized (via indium bump-bonding process) to a 640x512 pixel complementary metal-oxide semiconductor (CMOS) ROIC (Indigo System Corporation's ISC 9803) and is biased at $V_B = -1.1$ V. At temperatures below 72 K, the signal-to-noise ratio of the system is limited by array nonuniformity, readout multiplexer (i.e., ROIC) noise, and photocurrent (photon flux) noise. At temperatures above 72 K, the temporal noise due to the QWIP's higher dark current becomes the limitation. As mentioned earlier, this higher dark current is due to thermionic emission and thus causes the charge storage capacitors of the readout circuitry to saturate. Since the QWIP is a high impedance device, it should yield a very high charge injection coupling efficiency into the integration capacitor of the multiplexer. In fact, Bethea *et al.* [2] have demonstrated charge injection efficiencies approaching 90%. Charge injection efficiency can be obtained from [4] and is defined by

$$\eta_{inj} = \frac{g_m R_{Det}}{1 + g_m R_{Det}} \left[\frac{1}{1 + \frac{j\omega C_{Det} R_{Det}}{1 + g_m R_{Det}}} \right], \qquad (13)$$

where g_m is the transconductance of the MOSFET and it is given by $g_m = eI_{Det}/kT$. The differential resistance R_{Det} of the pixels at –1.1 V bias is 4.3×10^{10} Ohms at T = 65 K and detector capacitance $C_{Det} = 3.0 \times 10^{-14}$ F. The detector dark current I_{Det} = 1.5 pA under the same operating conditions. According to equation (13) the charge injection efficiency η_{inj} = 90% at a frame rate of 30 Hz. The FPA was back-illuminated through the flat thinned substrate membrane (thickness ≈ 1300 Å). This initial array gave excellent images with 99.92% of the pixels working (number of dead pixels ≈ 250), demonstrating the high yield of GaAs technology. The operability was defined as the percentage of pixels having NEDT less than 100 mK at 300 K background (with f/2 cold-stop) and in this case operability happens to be equal to the pixel yield.

We have used the following equation to calculate the NEDT of the FPA.

$$NEDT = \frac{\sqrt{A\Delta f}}{D_B^* (dP_B / dT) \sin^2(\theta/2)} \qquad (14)$$

where D_B^* is the blackbody detectivity (defined by equation (13)) and (dP_B / dT) is the change in the incident integrated blackbody power in the spectral range of detector with temperature. The integrated blackbody power P_B, in the spectral range from λ_1 to λ_2, can be written as

$$P_B = A \sin^2\left(\frac{\theta}{2}\right) \cos\phi \int_{\lambda 1}^{\lambda 2} W(\lambda) d\lambda, \qquad (15)$$

where blackbody spectral density respectively, and are defined

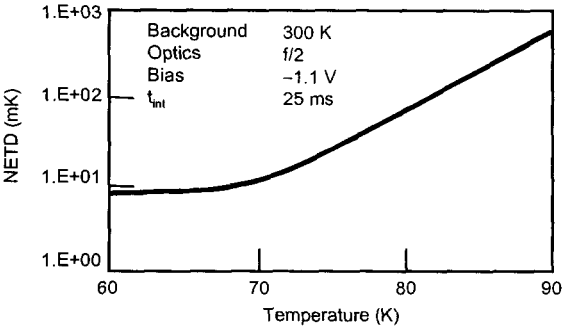

Fig. 7. Noise equivalent differential temperature NEDT estimated from test structure data as a function of temperature for bias voltage $V_B = -1.1$ V. The background temperature T_B = 300 K and the area of the pixel A = (23 μm)^2.

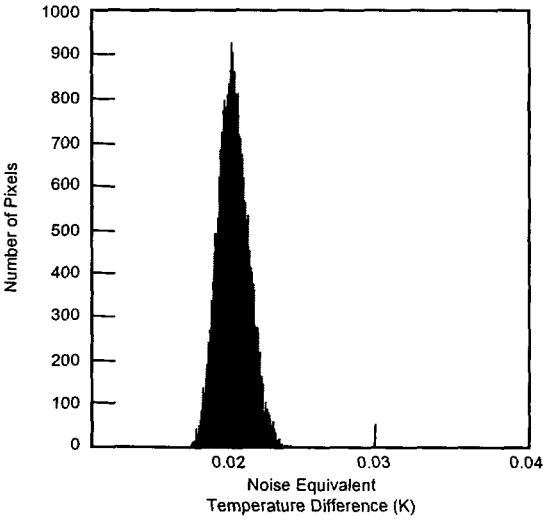

Fig. 8. NEDT histogram of the 327,680 pixels of the 640x512 array showing a high uniformity of the FPA. The uncorrected nonuniformity (= standard deviation/mean) of the FPA is only 5% including 1% nonuniformity of ROC and 1.4% nonuniformity due to the cold-stop not being able to give the same field-of-view to all the pixels in the FPA. The nonuniformity was reduced to an impressive 0.02% after two-point correction. No 1/f noise was observed down to 10 mHz.

by equations 16 and 17

$$P(\lambda) = W(\lambda)\sin^2(\theta/2)AF\cos\phi \quad (16)$$

where A is the detector area, ϕ is the angle of incidence, θ is the optical field-of-view angle [i.e., $\sin^2(\theta/2) = (4f^2+1)^{-1}$ where f is the f number of the optical system; in this case θ is defined by the radius ρ, of the blackbody opening at a distance D, from the detector, so that $\tan(\theta/2) = \rho/D$], F represents all coupling factors and $F = T_f(1\text{-}r)C$ where T_f is the transmission of filters and windows, r = 28% is the reflectivity of the GaAs detector surface, C is the optical beam chopper factor (C = 0.5 in an ideal optical beam chopper), and $W(\lambda)$ is the blackbody spectral density given by the following equation (i.e., the power radiated per unit wavelength interval at wavelength λ by a unit area of a blackbody at temperature T_B).

$$W(\lambda) = (2\pi c^2 h / \lambda^5)(e^{hc/\lambda kT_B} - 1)^{-1} \quad (17)$$

Figure 7 shows the NEDT of the FPA estimated from test structure data as a function of temperature for bias voltage V_B = –1.1 V. The background temperature T_B = 300 K, the area of the pixel A = (23 μm)^2, the f number of the optical system is 2, and the frame rate is 30 Hz. Figure 8 shows the measured NEDT histogram of the FPA at an operating temperature of T = 65 K, 16 msec integration time, bias V_B = –1.1 V for 300 K background with f/2 optics, and the mean value is 20 mK. This agrees reasonably well with our estimated value of 10 mK based on test detector data. The net peak quantum efficiency of the FPA was 1.5%, which also agrees closely with the single element test detector results. It is worth noting that under BLIP conditions the performance of the detectors is independent of the photoconductive gain, and depends only on the absorption quantum efficiency (as shown in equation (10)).

V. 640x512 PIXEL HAND-HELD CAMERA

A 640x512 QWIP FPA hybrid was integrated with a 330 mW integral Stirling closed-cycle cooler assembly and installed into an Indigo Phoenix™ camera-body to demonstrate a hand-held LWIR camera (shown in Fig. 9). The Phoenix™ infrared camera system has been developed by Indigo Systems Corporation to meet the needs of the research and industrial communities. The system is comprised of a camera head and a selection of two video processing back ends. The camera head consists of a 640x512 format LWIR QWIP array hybridized with an Indigo's ISC 9803 ROIC, a cold-stop, a Stirling cooler, pre-amplifiers, and analog-to-digital converters. The two video processing units are Real-Time Imaging Electronics (RTIE) that provide conventional NTSC video as well as corrected parallel digital video out at video rates and the Digital Acquisition System (DAS) that provides high-speed (40 MHz) raw digital data acquisition and output with limited real time video for system setup and focusing. The other element of the camera is a 100 mm focal length germanium lens, with a 9.2 degree field-of-view. It is designed to be transparent in the 7-14 μm wavelength range, to be compatible with the QWIP's 8.5 μm operation. The digital acquisition resolution of the camera is 14-bits, which determines the instantaneous dynamic range of the camera (i.e., 16,384). However, the dynamic range of QWIP is 85 dB. The nominal power consumption of the QWIP Phoenix™ hand-held camera is less than 45 W.

The measured mean NEDT of the QWIP camera system is 20 mK at an operating temperature of T = 65 K and bias V_B = –1.1 V for a 300 K background with germanium f/2 optics. The uncorrected photocurrent nonuniformity (which includes a 1% nonuniformity of the ROC and a 1.4% nonuniformity

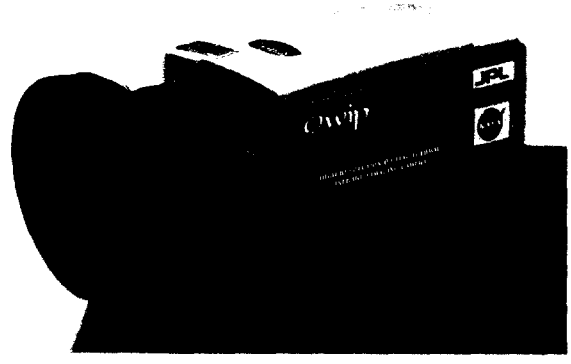

Fig. 9. Picture of the 640x512 hand-held long wavelength QWIP camera (QWIP Phoenix™).

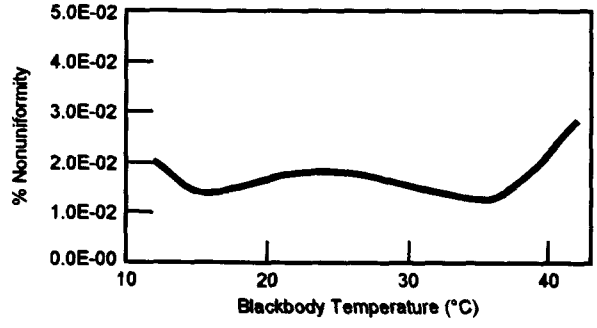

Fig. 10. Residual nonuniformity after two-point correction as a function of scene temperature. This corrected nonuniformity range is comparable to 3-5 μm infrared cameras.

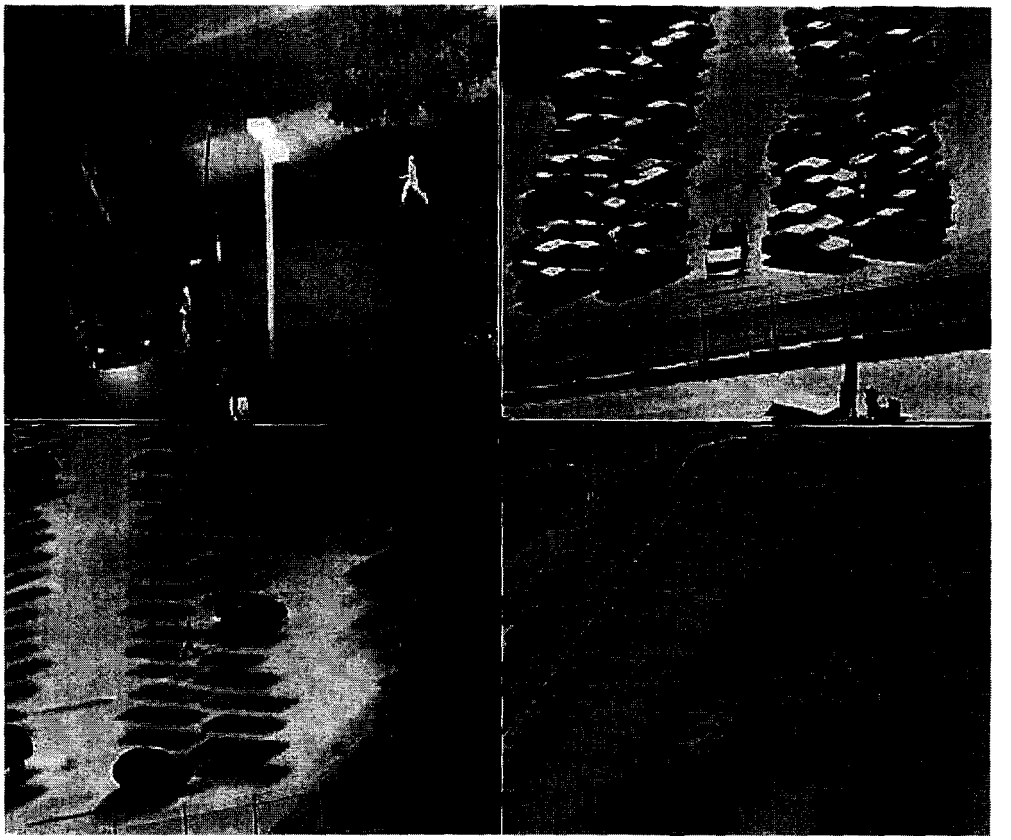

Fig. 11. Four frames of video images taken with the 9 μm cutoff 640x512 pixel QWIP Phoenix™ camera. These four images were taken at six-hour time intervals during a single day. Top left (6 AM), top right (noon), lower left (6 PM), and lower right (mid-night).

due to the cold-stop in front of the FPA not yielding the same field-of-view to all the pixels) of the 327,680 pixels of the 640x512 FPA is about 5% (= sigma/mean). The nonuniformity after two-point (17° and 27° Celsius) correction improves to an impressive 0.02%. As mentioned earlier, this high yield is due to the excellent GaAs growth uniformity and the mature GaAs processing technology. After correction, measurements of the residual nonuniformity were made at temperatures ranging from 12° Celsius (the cold temperature limit of the blackbody) up to 42° degrees Celsius. The nonuniformity at each temperature was found by averaging 64 frames, calculating the standard deviation of the pixel-to-pixel variation of the 64 frame average and then divided by the mean output, producing nonuniformity that may be reported as a percentage. For camera systems that have NEDT of about 20 mK, the corrected image must have less than 0.1% nonuniformity in order to be TV quality. Figure 10 shows the residual nonuniformity of the camera after two-point correction as a function of scene temperature. Also, it is clearly evident from Fig. 10 that the camera's performance is excellent in this scene temperature range, and its residual nonuniformity did not exceed 0.03% within the entire scene temperature range of 12° – 42° Celsius.

Video images were taken at a frame rate of 30 Hz at temperatures as high as T = 65 K, using a ROIC capacitor having a charge capacity of $11x10^6$ electrons (the maximum number of photoelectrons and dark electrons that can be counted in the time taken to read each detector pixel). Figure 11 shows four frames of video images taken with this large format LWIR camera at every six-hour time intervals within a day.

It should be noted that these initial unoptimized FPA results are far from optimum. The FPA performance data reported in this paper was taken with the first LWIR Phoenix™ camera. Estimates based on the single pixel data show that these FPAs should be able to provide 7 mK NEDT with 30 msec integration time, which can be achieved at $V_B = 1.1V$ bias. As shown in Fig. 8, the measured NEDT of the LWIR QWIP Phoenix™ camera is 20 mK with 16 msec integration time. The noise of the camera system can be written as, $N_{SYS}^2 = n_{Detector}^2 + n_{ADC}^2 + n_{MUX}^2$, where $n_{Detector}$ is the noise of the FPA, n_{ADC} is the noise of the analog-to-digital-converter, and n_{MUX} is the noise of the silicon ROIC. The experimentally

measured N_{SYS} is 2 units, and the n_{ADC} and n_{MUX} are 0.8 and 1 unit, respectively. This yields 1.5 noise units for $n_{Detector}$. Thus, the NEDT of the FPA is 15 mK at 300K background with f/2 optics and 16 msec integration time. Therefore, we should be able achieve 10.6 mK NEDT at the same operating conditions with 32 msec integration time.

VI. EFFECT OF FOCAL PLANE ARRAY NONUNIFORMITY

The general figure of merit that describes the performance of a large imaging array is the NEDT. NEDT is the minimum temperature difference across the target that would produce a signal-to-noise ratio of unity and is given by [16,17] equation (14). Before discussing the array results, it is also important to understand the limitations on the FPA imaging performance due to pixel nonuniformities. The total noise I_n of a focal plane array is given by,

$$I_n^2 = I_n^2 + u^2(I_P + I_D)^2 \tag{18}$$

where u is the nonuniformity of the FPA given by,

$$u = \frac{\sigma}{\mu} = \frac{\sigma}{I_P + I_D} \tag{19}$$

where μ is the mean total signal and σ is the standard deviation of the histogram of total signal versus number of pixels. Now the FPA detectivity or NEDT can be obtained by following equations,

$$D^*_{FPA} = \frac{R\sqrt{A\Delta f}}{I_n} \tag{20}$$

$$NEDT_{FPA} = \frac{\sqrt{A\Delta f}}{D^*_{FPA}(dP_B / dT)} \tag{21}$$

where I_n is the total noise of the FPA and is given by equation (18). The figures of merit such as D*, NEDT, NEP, NEI, etc. are different representations of the basic signal-to-noise ratio of radiation detectors normalized in different ways. The signal-to-noise ratio of a FPA can be written as,

$$SNR = \frac{I_P}{I_D} = \frac{I_P}{\sqrt{i_n^2 + u^2(I_P + I_D)^2}} \tag{22}$$

Under BLIP condition (use equation 12) this reduces to,

$$SNR \cong \frac{1}{u} \tag{23}$$

This analysis clearly shows the importance of the array uniformity in the FPA total signal-to-noise ratio. This point has been discussed in detail by Shepherd [18] for the case of PtSi infrared FPAs [19] which have low response, but very high uniformity. The general figure of merit to describe the performance of a large imaging array is NEDT, including the spatial noise which has been derived by Shepherd [18], and given by

$$NEDT = \frac{N_n}{dN_b / dT_b}, \tag{24}$$

where T_b is the background temperature and N_n is the total number of noise electrons per pixel, given by

$$N_n^2 = N_t^2 + N_b^2 + u^2 N_b^2. \tag{25}$$

The photoresponse independent temporal noise electrons are N_t, the shot noise electrons from the background radiation are N_b, and residual nonuniformity after correction by the electronics is u. The temperature derivative of the background flux can be written to a good approximation as

$$\frac{dN_b}{dT_b} = \frac{hcN_b}{k\bar{\lambda}T_b^2}, \tag{26}$$

where $\lambda = (\lambda_1 + \lambda_2)/2$ is the average wavelength of the spectral band between λ_1 and λ_2. When temporal noise dominates, NEDT reduces to equation (14). In the case where residual nonuniformity dominates, equations (24) and (26) reduce to

$$NEDT = \frac{u\bar{\lambda}T_b^2}{1.44}. \tag{27}$$

The units of the constant are cmK, $\bar{\lambda}$ is in cm and T_b is in K. Thus, in this spatial noise limited operation NEDT$\propto$u and higher uniformity means higher imaging performance. Levine [5] has shown as an example, taking T_b = 300 K, $\bar{\lambda}$ = 10 μm, and u = 0.1% leads to NEDT = 63 mK, while an order of magnitude uniformity improvement (i.e., u = 0.01%) gives NEDT = 6.3 mK. By using the full expression equation (25) Levine [5] has calculated NEDT as a function of D* and shown that when $D^* \geq 10^{10}$ cm$\sqrt{Hz}$ /W, the performance is uniformity limited and thus essentially independent of the detectivity [5].

VII. VERTICALLY INTEGRATED FOUR-COLOR QWIP DEVICE

This four-band vertically integrated device structure was achieved by the growth of multi-stack QWIP structures separated by heavily doped n^+ contact layers, on a GaAs substrate. Device parameters of each QWIP stack were designed to respond in different wavelength bands. Figure 12 shows the schematic device structure of a four-color QWIP FPA. A typical QWIP stack consists of a MQW structure of GaAs quantum wells separated by $Al_xGa_{1-x}As$ barriers. The actual device structure consists of a 15 period stack of 4-5 μm QWIP structure, a 25 period stack of 8.5-10 μm QWIP structure, a 25 period stack of 10-12 μm QWIP structure and a 30 period stack of 13-15.5 μm QWIP structure. Each photosensitive MQW stack was separated by a heavily doped n^+ (thickness 0.2 to 0.8 μm) intermediate GaAs contact layer (see Fig. 12). Since the dark current of this device structure is dominated by the longest wavelength portion of the device structure, the VLWIR QWIP structure has been designed to have a bound-to-quasibound intersubband absorption peak at 14.0 μm. Other QWIP device structures have been designed to have a bound-to-continuum intersubband absorption process because the photo current and dark current of these devices are relatively small compared to the VLWIR device. This whole four-band QWIP device structure was then sandwiched between 0.5 μm GaAs top and bottom contact layers doped with n = 5 x 10^{17} cm^{-3} and was grown on a semi-insulating GaAs substrate by MBE.

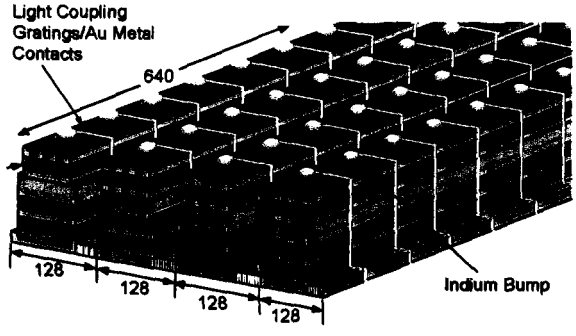

Fig. 12. Layer diagram of the four-band QWIP device structure and the deep groove two-dimensional periodic grating structure. Each pixel represent a 640x128 pixel area of the four-band focal plane array.

VIII. 640x512 PIXEL FOUR-COLOR SPATIALLY SEPARATED FOCAL PLANE ARRAY

In this section, we discuss the demonstration of the first 640x512 pixel monolithic spatially separated four-band QWIP FPA. The unique feature of this spatially separated four-band FPA is that the four infrared bands are independently and simultaneously readable on a single imaging array. This feature leads to a reduction in instrument size, weight, mechanical complexity, optical complexity and power requirements since no moving parts are needed. Furthermore, a single optical train can be employed, and the whole focal plane can operate at a single temperature.

The individual pixels of the four-color FPA were defined by photolithographic processing techniques (masking, dry etching, chemical etching, metal deposition, etc.). Four separate detector bands were defined by a deep trench etch process and the unwanted spectral bands were eliminated by a detector short-circuiting process. The unwanted top detectors were electrically shorted by gold-coated reflective two-dimensional etched gratings as shown in the Fig. 12. In addition to shorting, these gratings serve as light couplers for active QWIP stack in each detector pixel [20]. Design and optimization of these two-dimensional gratings to maximize QWIP light coupling are extensively discussed elsewhere [3]. The unwanted bottom QWIP stacks were electrically shorted at the end of each detector pixel row.

Typically, quarter-wavelength deep ($h = \lambda_p/4n_{GaAs}$) grating grooves are used for efficient light coupling in single-band QWIP FPAs. However, in this case, the height of the quarter-wavelength deep grating grooves is not deep enough to

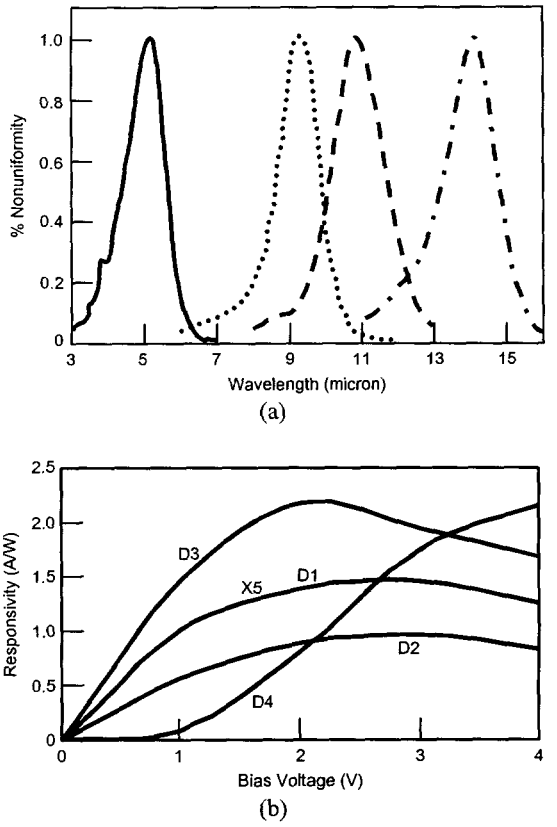

Fig. 13. (a) Normalized spectral response of the four-band QWIP FPA. (b) Bias dependent peak responsivities of the detectors in four-band QWIP FPA. The peak response wavelength for detectors D1, D2, D3, and D4 are $\lambda_p = 5$ μm, $\lambda_p = 9.1$ μm, $\lambda_p = 11.2$ μm, and $\lambda_p = 14.2$ μm, respectively. The responsivity curve for detector D1 is multiplied by a factor of 5 to fit to the scale.

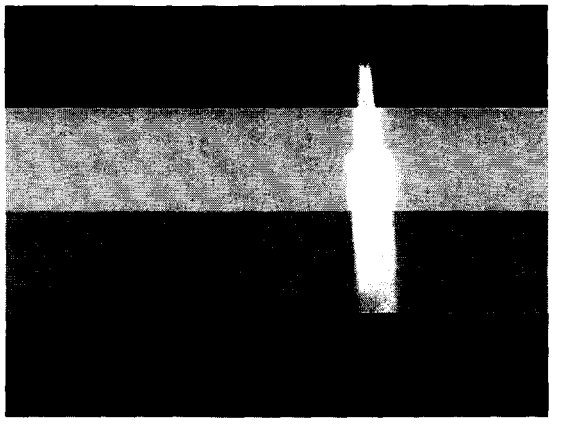

Fig. 14. One frame of video image taken with the 4-15.5 μm cutoff four-band 640x512 pixel QWIP camera. The image is barely visible in the 14-15.5 μm spectral band due to the poor optical transmission of the anti-reflection layer coated germanium lens.

short circuit the top three MQW QWIP stacks (e.g.: three top QWIP stacks on 14-15.5 μm QWIP in Fig. 12). Thus, three-quarter-wavelength groove depth two-dimensional gratings ($h = 3\lambda_p/4n_{GaAs}$) were used to short the top unwanted detectors over the 10-12 and 14-15.5 μm bands. This technique optimized the light coupling to each QWIP stack at corresponding bands while keeping the pixel (or mesa) height at the same level which is essential for the indium bump-bonding process used for detector array and readout multiplexer hybridization. Figure 13(a) shows the normalized spectral responsivities of all four spectral bands of this four-band FPA. Spectral band widths of the four detectors from shorter wavelength to longer wavelength in increasing order are $\Delta\lambda/\lambda_p \sim 26\%$, 15%, 17%, and 11%, respectively. Figure 13(b) shows the measured absolute responsivity at the peak wavelength for all four detectors. As expected, the narrower bandwidth and the flat responsivity near zero bias voltage indicate the bound-to-quasibound nature transition in the VLWIR detector [3,5]. Detectors in the 8.5-10 and 10-12 μm spectral-bands show a slightly broader spectral bandwidth, with increasing responsivity right at the beginning of the bias voltage, confirming the bound-to-continuum design [3,5]. The MWIR detector is specifically designed to cover a 4-5.5 μm wavelength range with $\Delta\lambda/\lambda_p \sim 26\%$ broader responsivity by utilizing three coupled quantum wells in each period of the MQW stack [12]. Also, the shorter wavelength response in this detector is achieved by using deeper $In_{0.33}Ga_{0.67}As$ quantum wells with lattice mismatched $Al_{0.3}Ga_{0.7}As$ barriers [12]. A high Al ratio is less desirable in these detectors because of the high defect density and the near crossing of the Γ and X valleys [3]. Also, the utilization of the coupled quantum wells within the MQW structure creates unbiased energy subbands where photexcited electrons can be easily relaxed before reaching the collector contact. These reasons could result in a very low optical responsivity in the MWIR detector as seen in the Figure 13(b).

A few QWIP FPAs were chosen and hybridized to a 640x512 pixel silicon CMOS ROIC (ISC 9803) and biased at $V_B = -1.5$ V. At temperatures below 83 K, the signal to noise ratio of the 4-5 μm spectral band is limited by array nonuniformity, multiplexer readout noise, and photo current (photon flux) noise. At temperatures above 45 K, temporal noise due to the 14-15.5 μm QWIP's higher dark current becomes the limitation. The 8-10 and 10-12 μm spectral bands have shown BLIP performance at temperatures between 45 and 83 K. The FPAs were back-illuminated through the flat thinned substrate membrane (thickness ≈ 1300 Å). This initial array gave excellent images with 99.9% operability (number of dead pixels ≈ 250). As mentioned earlier, this success is mostly due to the mature GaAs growth and processing technologies.

A 640x512 pixel four-band QWIP FPA hybrid was mounted onto a 84-pin lead-less chip carrier and installed into a laboratory dewar which is cooled by liquid helium to demonstrate a 4-band simultaneous imaging camera. The FPA was cooled to 45 K and the temperature was stabilized by a temperature controller and regulating the pressure of gaseous helium. The other element of

the FPA test setup is a 100 mm focal length anti-reflection coated germanium lens, which gives a 9.2° field-of-view. The anti-reflective coating is optimized to be transparent in the 8-12 μm wavelength range. SEIR™ image processing station was used to obtain clock signals for readout multiplexer and to perform digital data acquisition and nonuniformity corrections. The digital data acquisition resolution of the camera is 14-bits, which determines the instantaneous dynamic range of the camera (i.e., 16,384). Video images were taken at a frame rate of 30 Hz at temperatures as high as T = 45 K, using a ROIC capacitor having a charge capacity of $11x10^6$ electrons. Figure 14 shows one frame of a video image taken with the four-band 640x512 pixel QWIP FPA. It is noticeable that the object in the 13-15.5 μm band is not very clear due to the reduced optical transmission of the germanium lens beyond 14 μm.

The dark current vs. bias voltage of the detector test mesas was measured at different temperatures. Figure 15 shows the pixel level dark currents vs. temperature at the operating bias voltage $V_B = -1.5V$, and as expected, the VLWIR detector shows the highest dark current level. The peak detectivities of all four bands at a 300K background with f/5 optics were estimated using equations (3) an (7). Figure 16 shows the peak detectivities of all four spectral-bands as a function of operating temperature. Based on this single element test detector data, the 4-5, 8-12, 10-12, and 13.5-15.5 μm spectral bands show BLIP at temperatures 40, 50, 60 and 120 K, respectively, for a 300 K background with a f/5 cold stop. As expected (due to BLIP), the estimated and experimentally obtained NEDT values of all spectral-bands do not change significantly below their BLIP temperatures. The experimentally measured NEDT of 4-5, 8-12, 10-12, and 13.5-15.5 μm detectors at 40 K are 21.4, 45.2, 13.5, and 44.6 mK, respectively (see Fig. 17). These experimentally measured NEDT agree reasonably well with the estimated NEDT values based on the single element test detector data [21].

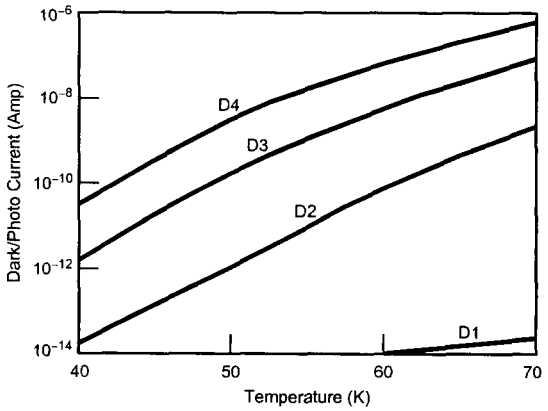

Fig. 15. Dark currents detectors D1, D2, D3, and D4 of the four-band FPA at bias $V_B = -1.5$ V as a function of operating temperature.

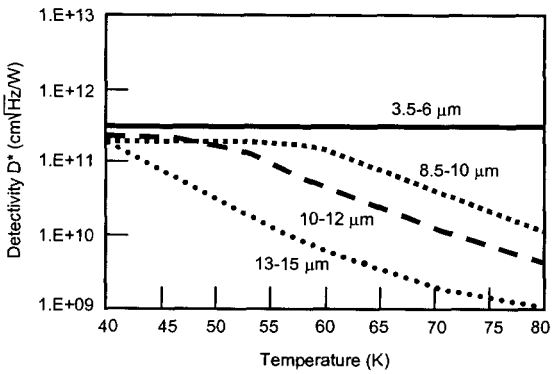

Fig. 16. Detectivities of each spectral-band of the four-band QWIP FPA as a function of temperature. Detectivities were estimated using the single pixel test detector data taken at $V_B = -1.5$ V and 300 K background with f/5 optics.

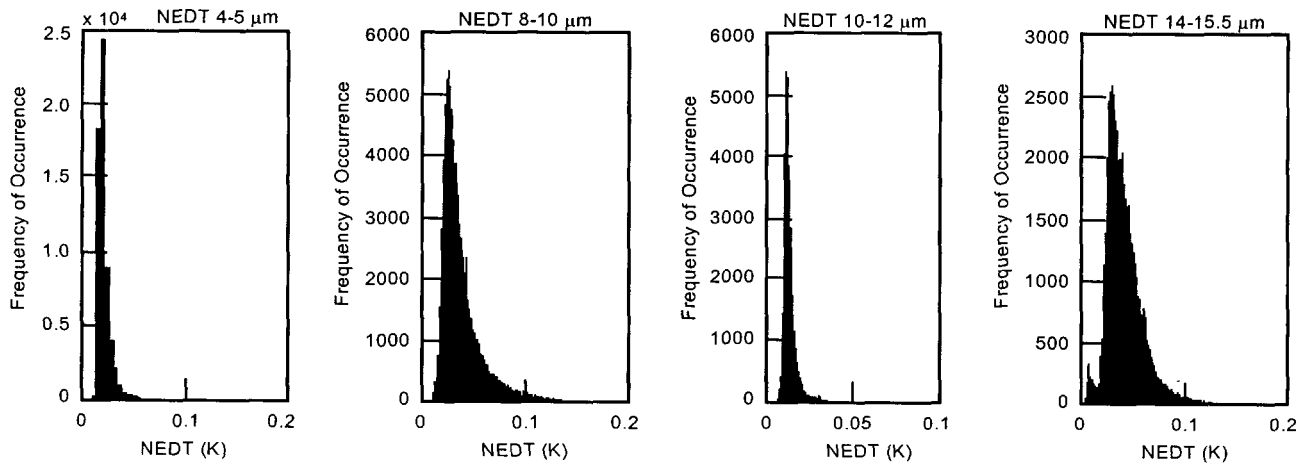

Fig. 17. NEDT histogram of the 640x512 pixel spatially separated four-band focal plane showing a high uniformity of the FPA. Each spectral band of the FPA consisted of 640x128 pixels. The experimentally measured NEDT of 4-5, 8-12, 10-12, and 13.5-15.5 μm detectors at 40 K are 21.4, 45.2, 13.5, and 44.6 mK, respectively.

IX. BROAD-BAND QWIP DEVICE

The broadband QWIP device structure was designed by repeating a unit of several quantum wells with slightly different parameters such as well width and barrier height [22]. The positions of ground and excited states of the quantum well are determined by the quantum well width (L_w) and the barrier height, i.e. the Al mole fraction (x) of the barrier. Since each single set of parameters for a bound-to-quasibound quantum well [3] corresponds to a spectral band pass of about 1.5 μm, three different sets of values are sufficient to cover a 10-16 μm spectral region (see Fig. 18). The MQW structure consists of many periods of these three-quantum-well units separated by thick barriers [22,23].

The device structure reported here involved 33 repeated layers of GaAs three-quantum-well units separated by $L_B \sim 575$ Å thick $Al_xGa_{1-x}As$ barriers. The well thickness of the quantum wells of three-quantum-well units are designed to respond at peak wavelengths around 13, 14, and 15μm, respectively. These wells are separated by $L_u \sim 75$ Å thick $Al_xGa_{1-x}As$ barriers. The Al mole fraction (x) of barriers throughout the structure was chosen such that the $\lambda_p = 13$ μm quantum well operates under bound-to-quasibound conditions. The excited state energy level broadening has been further enhanced due to the overlap of the wavefunctions associated with excited states of quantum wells separated by thin barriers [22,23]. Energy band calculations based on a two band model show excited state energy levels spreading about 28 meV.

The sample was grown on a semi-insulating 3-inch GaAs substrate by using MBE growth technique. It consists of the device structure described above sandwiched between top and bottom contact layers. Transport carriers (electrons) were provided by doping all GaAs wells and contact layers with Si. In order to measure the dark current-temperature curve, spectral responsivity (see Figure 19-20), and noise, 200 μm diameter mesas were fabricated using wet chemical etching and Au/Ge ohmic contacts were evaporated onto the top and bottom contact layers.

The responsivity spectra of these detectors were measured using a 1000 K blackbody source and a grating monochromator. The detectors were back illuminated through a 45° polished facet to obtain normalized responsivity spectra at different bias voltages. Then the absolute spectral responsivities were obtained by measuring total photocurrent from a calibrated blackbody source. In Fig. 20(a), the responsivity curve at $V_B = -2.5$ V bias voltage shows broadening of the spectral response up to $\Delta\lambda \sim 5.5$ μm, (i.e. the full-width at half-maximum from 10.5 – 16 μm). This broadening $\Delta\lambda/\lambda_p \sim 42$ % is about a 400% increase compared to a typical bound-to-quasibound QWIP.

Unlike narrow-band QWIPs, these detectors show spectral peak shifts from $\lambda = 11.5$ μm to $\lambda = 15.1$ μm as negative bias voltage increased from $V_B = -1$ V to $V_B = -5$ V and similar behavior (λ

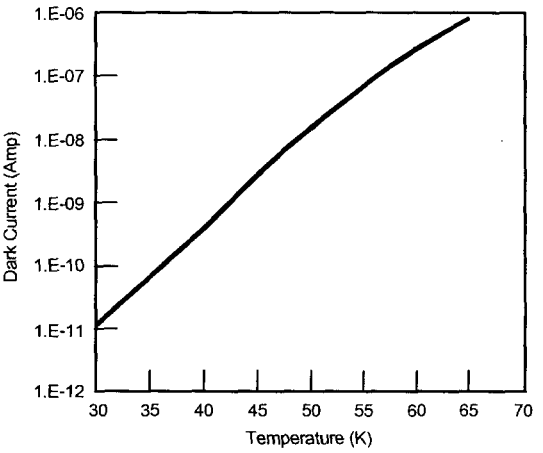

Fig. 19. Dark current-temperature curve of 10-15.4 μm broadband QWIP at bias $V_B = -2.5$V. Data were taken with a 200 μm diameter test structure and normalized to 25x25 μm^2 pixel.

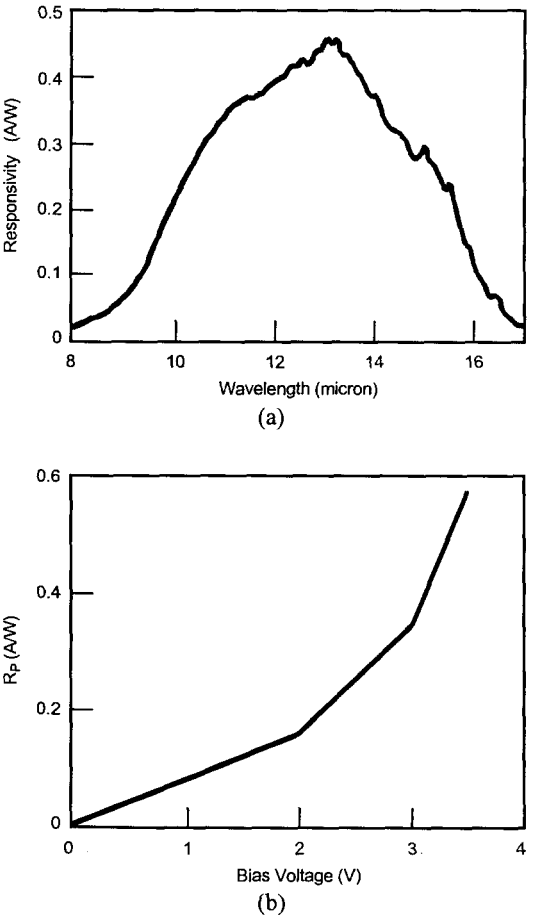

Fig. 20. (a) Responsivity spectrum of a broadband QWIP test structure at temperature T = 55 K. The spectral response peak is at 13.5 μm and the long wavelength cutoff is at 15.4 μm. (b) Peak responsivity as a function of bias voltage at temperature T = 55 K.

= 11.5 μm to λ = 14.7 μm for V_B = +1 V to V_B = +5 V) was observed under positive bias voltages as well. This suggests that there is no substantial carrier depletion due to the applied electric field within the three-quantum-units because the direction of peak shift remains the same under both positive and negative biases. The responsivity of the detector peaks at 13.5 μm and the peak responsivity (R_p) of the detector is 250 mA/W at bias V_B = –2.5 V. The bias dependent peak responsivity of the detector is shown in Fig. 20(b). The measured absolute peak responsivity of the detector is small, up to about V_B = –0.5 V. Beyond that it increases nearly linearly with bias reaching R_P = 580 mA/W at V_B = –3.5 V. This type of behavior of responsivity versus bias is typical for a bound-to-quasibound QWIP. The peak quantum efficiency was 11% at bias V_B = –2.5 V for a 45° double pass.

The dark current noise i_n of the device was measured using a spectrum analyzer at T = 55 K as a function of bias voltage. The photoconductive gain g can now be obtained using the generation-recombination noise calculated based on standard noise expression given in equation (7). Using experimental measurements of noise and responsivity, one can now calculate specific detectivity D^* using equation (3). The calculated D* value for the present device (λ = 15.4 μm) at T = 55 K and V_B = 2.5 V is 3 x 10^{10} cm$\sqrt{\text{Hz}}$ /W. Even with broader response, this D^* is comparable to previously reported D^* of QWIPs with narrow spectral response. Figures 21 and 22 show the detectivity D* and the NEDT as a function of the operating temperature of the device.

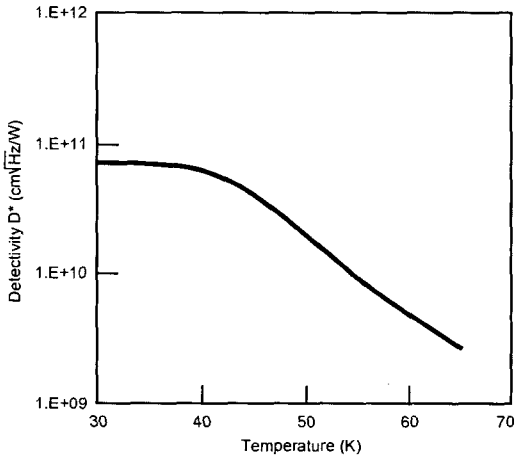

Fig. 21. Detectivity as a function of temperatures at bias voltage V_B = –2.5V.

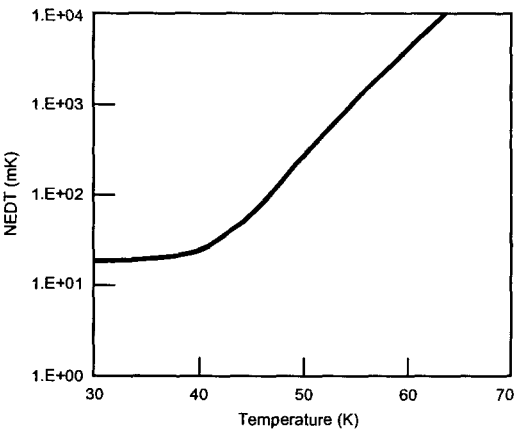

Fig. 22. Noise equivalent temperature difference as a function of temperatures at bias voltage V_B = –2.5V.

X. 640x512 PIXEL BROAD-BAND QWIP FOCAL PLANE ARRAY

Though two-dimensional grating is an efficient light coupler, it is not suitable for broad-band QWIPs due to its inherent narrow band light coupling efficiency. Thus, we have implemented a wide-ranged random reflector for coupling normal incident radiation into broad-band QWIPs. This random structure was fabricated on the detectors by using standard photolithography and Cl_2-based reactive ion etching. The advantage of the photolithographic process over a completely random process is the ability to accurately control the feature size and preserve the pixel-to-pixel uniformity which is a prerequisite for high sensitivity imaging FPAs.

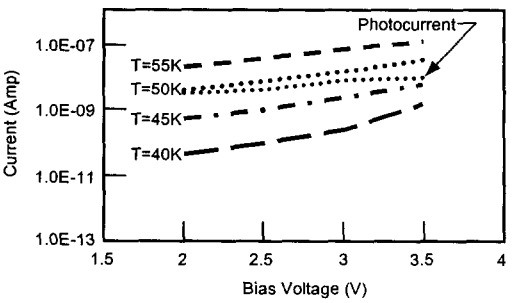

Fig. 23. Dark current and the photocurrent of 10-15.4 μm broadband QWIP as a function of bias voltage.

The random reflector array was defined by the lithography and dry etching. Photoconductive QWIPs of the 640x512 pixel FPAs were then fabricated by dry etching through the photosensitive GaAs/$Al_xGa_{1-x}As$ MQW layers into the 0.5 μm thick doped GaAs bottom contact layer. The pixel pitch of the FPA is 25 μm and the actual pixel size is 23x23 μm^2. The random reflectors on top of the detectors were then covered with Au/Ge and Au for Ohmic contact and reflection. Indium bumps were then evaporated on top of the detectors for hybridization with silicon ROIC. A single QWIP FPA was chosen and hybridized (via indium bump-bonding process) to a 640x512 pixel silicon CMOS ROIC (ISC 9803) and biased at V_B = –2.5 V. At temperatures below 48 K, the signal to noise ratio of the system is limited by array nonuniformity, multiplexer readout noise, and photo current (photon flux) noise (see Figure 23). At temperatures above 48 K, temporal noise due to the QWIP's higher dark current becomes the limitation. As mentioned earlier this higher dark current is due to thermionic emission and thus

causes the charge storage capacitors of the readout circuitry to saturate. Since the QWIP is a high impedance device, it should yield a very high charge injection coupling efficiency into the integration capacitor of the multiplexer.

Equation (13) was used to estimate the charge injection efficiency. The differential resistance R_{Det} of the pixels at –2 V bias is 5.4×10^{10} Ohms at T=45 K and detector capacitance $C_{Det} = 1.4 \times 10^{-14}$ F. The detector dark current $I_{Det} = 8$ pA under the same operating conditions. According to equation (13) the charge injection efficiency $\eta_{inj} = 99.5\%$ at a frame rate of 30 Hz. The FPA was back-illuminated through the flat thinned substrate membrane (thickness ≈ 2000 Å). As described earlier this thinned GaAs FPA membrane has completely eliminated the thermal mismatch between the silicon CMOS ROIC and the GaAs based QWIP FPA, and has completely eliminated the pixel-to-pixel optical cross-talk of the FPA. This initial array gave very good images with 99.9% operability.

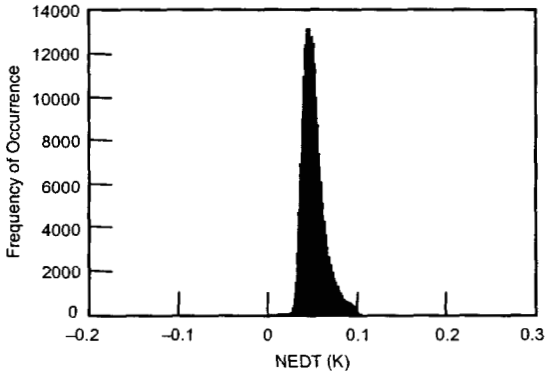

Fig. 24. Noise equivalent temperature difference (NEDT) histogram of the 327,680 pixels of the 640x512 array showing high uniformity of the FPA. The uncorrected nonuniformity (= standard deviation/mean) of this unoptimized FPA is only 6.3% including 1% nonuniformity of the ROC and a 1.4% nonuniformity due to the cold-stop not being able to give the same field-of-view to all the pixels in the FPA.

Equation (14) was used to calculate the NEDT of the FPA. The background temperature $T_B = 300$ K, the area of the pixel A = (23 μm)^2, the f number of the optical system is 2, and the frame rate is 30 Hz. Figure 24 shows the experimentally measured NEDT histogram of the FPA at an operating temperature of T = 35 K, bias $V_B = -2.5$ V at 300 K background with f/2 optics and the mean value is 55 mK. This agrees reasonably well with our estimated value of 25 mK based on test structure data. The read noise of the multiplexer is 500 electrons. The factor of two shortfall of NEDT is mostly attributed to decrease in bias voltage across the detectors during charge accumulation (common in many direct-injection type readout multiplexers) and read noise of the readout multiplexer. The experimentally measured peak quantum efficiency of the FPA was 9.5%, which agrees well with the 11% quantum efficiency estimated from the single element detector data. A 640x512 pixel QWIP FPA hybrid was mounted onto an 84-pin lead-less chip carrier and installed into a laboratory dewar which is cooled by liquid neon to demonstrate a LWIR imaging camera (FPA was cooled to 35K). We have used a 100 mm focal length anti-reflection coated germanium lens with a 9.2° field-of-view for imaging. It is designed to be transparent in the 8-12 μm wavelength range (which is not fully compatible with the 10-15 μm broadband QWIP array). The measured mean NEDT of the QWIP camera is 55 mK at an operating temperature of T = 35 K and bias $V_B = -2.5$ V at 300 K background with f/2 optics (see Fig. 24). This is in good agreement with expected FPA sensitivity due to the practical limitations on the charge handling capacity of the multiplexer, read noise, bias voltage, and operating temperature. The uncorrected NEDT nonuniformity of the 327,680 pixels of the 640x512 FPA is about 6.3% (= sigma/ mean). The nonuniformity after two-point (17° and 27° Celsius) correction improved to 0.1%.

In summary, we have demonstrated a very sensitive 640x512 pixel portable LWIR imaging camera. We also have discussed the demonstration of the first 640x512 pixel spatially separated monolithic four-band detector array and the first 640x512 pixel broad-band FPA. These can be used in many ground based and space borne applications that require long-wavelength, large, uniform, reproducible, and low 1/f noise [8] narrow-band, multi-band, and broad-band LWIR FPAs. These initial 640x512 pixel narrow-band, four-band, and broad-band QWIP FPAs have shown excellent performance, stability, operability, and yields.

ACKNOWLEDGMENTS

The authors would like to express their gratitude to C. P. Bankston, M. Bothwell, T. Krabach, and P. Grunthaner for the encouragement and support during the development novel QWIP FPAs at the Jet Propulsion Laboratory for various applications. Also, authors would like to give their special thanks to F. Reininger of the Jet Propulsion Laboratory, J. Woolaway and C, Shott of the Indigo System Corporation, M. Jhabvala of the NASA Goddard Space Flight Center, and K. K. Choi of Army Research Laboratory for stimulating technical discussions. The research described in this paper was performed by the Jet Propulsion Laboratory, California Institute of Technology, and was jointly sponsored by the Breakthrough Sensors and Instrument Component Technology Thrust of the NASA Cross-Enterprise Technology Development Program and the NASA Earth Science Technology Office.

REFERENCES

[1] C. Weisbuch, *Semicon. Semimet.*, vol. 24, Academic Press, 1987, pp.1-133.

[2] C. G. Bethea, B. F. Levine, V. O. Shen, R. R. Abbott, and S. J. Hseih, IEEE Trans. Electron Devices,"10 μm GaAs/AlGaAs Multiquantum Well Scanned Array Infrared Imaging Camera", vol. 38, pp 1118-1123, 1991.

[3] S. D. Gunapala and S. V. Bandara, "Quantum Well Infrared Photodetector (QWIP) Focal Plane Arrays," *Semicon. Semimet.*, vol. 62, H. C. Liu and F. Capasso, Ed. San Diego: Academic Press, 2000, pp. 197-282.

[4] C. G. Bethea, B. F. Levine, M. T. Asom, R. E. Leibenguth, J. W. Stayt, K. G. Glogovsky, R. A. Morgan, J. Blackwell, and W. Parish, "Long Wavelength Infrared 128x128 $Al_xGa_{1-x}As$/GaAs Quantum Well Infrared Camera and Imaging System", IEEE Trans. Electron Devices, vol. 40, pp. 1957-1963, 1993.

[5] B. F. Levine, "Quantum-well infrared photo-detectors", J. Appl. Phys., Vol. 74, R1-R81, 1993.

[6] H. Schneider, P. Koidl, M. Walther, J. Fleissner, R. Rehm, E. Diwo, K. Schwarz, and G. Weimann, "Ten years of QWIP development at Fraunhofer IAF", Infrared Physics and Technology, vol. 42, pp. 283-290, 2001.

[7] B. Hirschauer, J. Alverbro, J. Andersson, J. Borglind, A. Bustamante, Z. Fakoor-Biniaz, U. Halldin, P. Halander, Y. Lindberg-Erikson, H. Malm, H. Martijn, C. Nordahl, and O. Oberg, "Development and production of QWIP focal plane arrays at ACREO", Infrared Physics and Technology, vol. 42, pp. 329-332, 2001.

[8] Sarath D. Gunapala, John K. Liu, Jin S. Park, Mani Sundaram, Craig A. Shott, Ted Hoelter, True-Lon Lin, S. T. Massie, Paul D. Maker, Richard E. Muller, and Gabby Sarusi" 9 μm Cutoff 256x256 GaAs/$Al_XGa_{1-X}As$ Quantum Well Infrared Photodetector Hand-Held Camera", IEEE Trans. Electron Devices, vol. 44, pp. 51-57, 1997.

[9] H. C. Liu, "Quantum Well Infrared Photodetector Physics and Novel Devices", *Semicon. Semimet.*, vol. 62, H. C. Liu and F. Capasso, Ed. San Diego: Academic Press, 2000, pp. 126-196.

[10] Sarath D. Gunapala, Sumith V. Bandara, John K. Liu, Winn Hong, Mani Sundaram, Paul D. Maker, Richard E. Muller, Craig A. Shott, and Ronald Carralejo, "Long-Wavelength 640x486 GaAs/$Al_xGa_{1-x}As$ Quantum Well Infrared Photodetector Snap-shot Camera", IEEE Trans. Electron Devices, vol. 45, pp. 1890-1895, 1998.

[11] J. Y. Andersson, J. Alverbro, J. Borglind, P. Helander, H. Martijn, and M. Ostlund, "320x240 Pixels Quantum Well Infrared Photodetector (QWIP) Array for Thermal Imaging: Fabrication and Evaluation", SPIE 3061, pp. 740-748, 1997.

[12] K. K. Choi, S. V. Bandara, S. D. Gunapala, W. K. Liu, and J. M. Fastenau, J. Appl. Phys., "Detection wavelength of InGaAs/AlGaAs quantum wells and superlattices", vol. 91, pp. 551-564, 2002.

[13] R. Breiter, W. Cabanski, R. Koch, W. Rode, and J. Ziegler, "Recent development for QWIP IR imaging modules at AIM", SPIE, vol. 3379, pp. 423-432, 1998.

[14] G. Sarusi, B. F. Levine, S. J. Pearton, K. M. S. Bandara, and R. E. Leibenguth, "Improved perfor-mance of quantum well infrared photodetectors using random scattering optical coupling", Appl. Phys. Lett., vol. 64, pp. 960-962, 1994.

[15] S. D. Gunapala and S. V. Bandara, "GaAs/AlGaAs based quantum well infrared photodetector focal plane arrays," Handbook of Infrared Detection Technologies, M. Henini and M. Razeghi, Ed. London: Elsevier, 2002, pp. 83-117.

[16] R. H. Kingston, *Detection of Optical and Infrared Radiation* (Springer, Berlin), 1978.

[17] A. Zussman, B. F. Levine, J. M. Kuo, and J. de Jong, "Extended long-wavelength λ=11-15 μm GaAs/ $Al_xGa_{1-x}As$ quantum-well infrared photodetectors", J. Appl. Phys., Vol.70, 5101-5107, 1991.

[18] F. D. Shepherd, "Silicide infrared staring sensors", SPIE, vol. 930, pp.2-10, 1988.

[19] J. M. Mooney, F. D. Shepherd, W. S. Ewing, J. E. Murgia, and J. Silverman, "Responsivity nonuni-formity limited performance of infrared staring cameras", Opt. Eng. 28, 1151-1161, 1989.

[20] Sarath D. Gunapala, Sumith V. Bandara, A. Singh, John K. Liu, Sir B. Rafol, E. M. Luong, Jason M. Mumolo, Nhan Q. Tran, David Z.-Y. Ting, J. D. Vincent, Craig A. Shott, J. Long, and Paul D. LeVan, "640x486 Long-Wavelength Two-Color GaAs/AlGaAs Quantum Well Infrared Photodetector (QWIP) Focal Plane Array Camera", IEEE Transactions on Electron Devices, vol. 47, pp. 963-971, 2000.

[21] M. Jhabvala, "Applications of GaAs quantum well infrared photoconductors at the NASA/Goddard Space Flight Center", Infrared Physics and Technology, vol. 42, pp. 363-376, 2001.

[22] S. V. Bandara, S. D. Gunapala, J. K. Liu, E. M. Luong, J. M. Mumolo, W. Hong, D. K. Sengupta, and M. J. McKelvey, "10-16 μm Broadband Quantum Well Infrared Photodetector", Appl. Phys. Lett., Vol. 72, pp. 2427-2429, 1998.

[23] S. V. Bandara, S. D. Gunapala, J. K. Liu, E. M. Luong, J. M. Mumolo, W. Hong, D. K. Sengupta, and M. J. McKelvey, "10- to 16-μm Broadband Quantum Well Infrared Photodetector", SPIE, vol. 3379, pp. 396-401, 1998.